

On the Microlensing Optical Depth of the Galactic Bar

HongSheng Zhao and Shude Mao ^{*}

Max-Planck-Institute für Astrophysik, Karl-Schwarzschild-Strasse 1, 85740 Garching, Germany

Accepted Received; in original form

ABSTRACT

The microlensing probability (optical depth τ) toward the Galactic center carries information about the mass distribution of the Galactic bulge/bar, so can be used to constrain the very uncertain shape parameters of the Galactic bar. In this paper we study a family of bar models with tunable triaxiality, boxyness and radial profile to span the range of plausible density models of the Galactic bar. It also includes four models that were used to fit to the COBE maps by Dwek et al (1995). We find the optical depth on the minor axis of the whole family of models and in special cases the whole microlensing map of the bulge/bar are given by simple analytical formulae. The formulae show the following dependence of the optical depth on the bar mass, radial profile, angle, axis scale lengths and boxyness.

- (1) τ is proportional to the mass of the bar, M .
- (2) τ falls along the minor axis with a gradient determined by the density profile and boxyness of the bar.
- (3) Going from an oblate bulge to a triaxial bar, the optical depth increases only if $\alpha < 45^\circ$, where α is the angle between the bar's major axis and our line of sight to the center.
- (4) Among bars with different degree of triaxiality, τ is the largest when the bar axis ratio $\frac{y_0}{x_0} = \tan \alpha$, where y_0, x_0 are the bar scale lengths on the short and long axes in the Galactic plane respectively.
- (5) At a fixed field on the minor axis but away from the center, boxy bars with a flat density profile tend to give a larger optical depth than ellipsoidal bars with a steep profile.
- (6) Main sequence sources should have a significantly lower (20-50% lower)

arXiv:astro-ph/9605030v1 7 May 1996

optical depth than red clump giants if main sequence stars are not observed as deep as the bright clump giants.

For the four COBE-constrained models, the optical depths contributed by the bar is in the range of $\approx (0.3 - 2.2) \times 10^{-6} M / (2 \times 10^{10} M_{\odot})$ at Baade window. Out of the four models, only the model with a Gaussian profile and ellipsoidal shape satisfies the observational constraint, the other three models produce optical depths which are inconsistent or marginally consistent with the 2σ lower limit of the observed optical depths, even if we adopt both a massive bar $2.8 \times 10^{10} M_{\odot}$ and a full disk. Independent of the COBE map, we find that the microlensing models can potentially provide constraints on the mass distribution. If increasing microlensing statistics confirm the high optical depth, $\approx 3 \times 10^{-6}$, presently observed by the MACHO and OGLE collaborations, then the observation argues for a massive ($\geq 2 \times 10^{10} M_{\odot}$) boxy bar with axis ratio $\frac{y_0}{x_0} \approx \tan(\alpha)$ and $\alpha \leq 20^\circ$ and with a flat radial profile up to corotation. Stronger limits on the bar parameters can be derived within two years when the sample is increased from the current fifty events to about two hundred events.

Key words: dark matter - gravitational lensing - galactic centre

1 INTRODUCTION

Microlensing surveys such as the MACHO (Alcock et al. 1993, 1995a, b), OGLE (Udalski et al. 1993, 1994), EROS (Aubourg et al. 1993) and DUO (Alard et al. 1995) collaborations have discovered more than 100 microlensing events toward the Galactic bulge and about 10 events toward the LMC. One of the many exciting discoveries (see Paczyński 1996 for a review) is the surprisingly high optical depth, τ , i.e., microlensing probability, toward the Galactic centre (Udalski et al. 1994; Alcock et al. 1995b). The OGLE collaboration found $\tau_{-6} \equiv \tau/10^{-6} = (3.3 \pm 2.4)$ (2σ error bar) based on 9 events and the MACHO collaboration found $\tau_{-6} = 2.43_{-0.74}^{+0.9}$ (2σ) based on the full sample of 41 events and $\tau_{-6} = 6.32_{-3.57}^{+6}$ (2σ) for 10 low latitude clump giants. This is clearly in excess of all the predictions prior to the discovery of microlensing events (Kiraga & Paczyński 1994a). Both a maximum disk (Gould 1994a, Alcock et al. 1995b) and a Galactic bar oriented roughly toward us (Paczyński et al. 1994a; Zhao, Spergel & Rich 1995, Zhao, Rich & Spergel 1996, hereafter ZSR95, ZRS96)

* E-mail: (hsz, smao)@mpa-garching.mpg.de

have been proposed as an explanation. The latter interpretation is favored by other lines of evidence, such as the non-circular motion of gas in the inner Galaxy (Binney et al. 1991; Blitz & Spergel 1991), the asymmetric and boxy COBE map (Weiland et al. 1995) and that the clump giants appear brighter at one side ($l > 0^\circ$) than the other side ($l < 0^\circ$) of the bulge (Stanek et al. 1994). A Galactic bar, together with a normal disk, can produce an optical depth $\tau_{-6} \approx 2.5$ (ZSR95, ZRS96). This value is in good agreement with the OGLE and the MACHO full sample values, but seems to be at the 2σ lower limit of that for the 10 low latitude clump giants in the MACHO sample. The theoretical prediction depends on the still uncertain bar axial ratio, orientation and mass profile; Dwek et al. (1995) found that several bar volume density models are consistent with the COBE map. Given these uncertainties, what is the range of the predicted optical depth? What are the optimal bar configurations that can produce an optical depth as high as $\tau_{-6} = 6$? Can the Galactic microlensing observations put constraints on the bar parameters? These are the main questions we want to address in the paper. We demonstrate that the published optical depth based on about 10 microlensing events with red clump giants as sources already put interesting constraints on the orientation, axial ratio and boxyness of the bar. With steadily increasing number of events and decreasing error bar for the optical depth, microlensing will become a very powerful tool to probe the Galactic structure.

The outline of the paper is as follows. In §2, we study a family of models for the bar density distribution, which includes many models used in the literature. We derive an analytical expression of their optical depths on the minor axis and for ellipsoidal bars the whole microlensing map on the sky as well. In §3, we apply our formalism to the Galactic bar, and compare the results with the observations. We summarize our results and discuss the implications in §4. More mathematical details are given in the appendices and at the end of Appendix C some instructions of using our formulae.

2 MODEL

In this section we first give the general expressions for the microlensing probability (optical depth) of a bar, then derive the optical depth map for a simple ellipsoidal Gaussian bar model. The results are then extended to a family of bar models with more general shapes and radial profiles. Using these models we study the dependence of the optical depth on parameters of the bar.

2.1 Microlensing Optical Depth of the Bar

The microlensing optical depth for a source at distance D_s is the probability for it to come within one Einstein radius of any lens (deflector) placed at $0 < D_d < D_s$:

$$\tau(D_s) = \int_0^{D_s} \left(\frac{\rho(D_d)}{m} \right) (\pi R_E^2) dD_d, \quad R_E \equiv \left(\frac{4GmD}{c^2} \right)^{1/2}, \quad D \equiv (D_s - D_d) \frac{D_d}{D_s}, \quad (1)$$

where m is the mass of the lens, $\rho(D_d)$ is the mass density of the lens at distance D_d , R_E is the Einstein radius, D is the effective distance between the lens and the source, c is the speed of light and G is the gravitational constant. The first bracketed term is the number density of the source at distance D_d , while the second term gives the lensing cross section, namely, the area enclosed by one Einstein radius. Note that the lens mass m cancels out, therefore the optical depth depends only on the total mass density of the lenses, but not on the mass spectrum.

The microlensing optical depth is usually measured for all sources in a narrow cone of the sky (e.g., Baade window of the bulge, $l = 1^\circ$, $b = -3.9^\circ$), therefore it is necessary to take into account the distribution of source distances by averaging over the line of sight:

$$\langle \tau \rangle = \frac{\int_0^{s_{max}} \tau(D_s) n(D_s) dD_s}{\int_0^{s_{max}} n(D_s) dD_s}, \quad n(D_s) dD_s \propto \rho(D_s) D_s^{2-2\beta_s} dD_s, \quad (2)$$

where $D_{s,max}$ is the maximum distance of an observable source, and $n(D_s)dD_s$ is the number of observable sources at distance D_s to $D_s + dD_s$ in the field of view. The factor of D_s^2 in $n(D_s)$ takes into account the volume increase with distance for a fixed field of view, and the factor $D_s^{-2\beta_s}$ parametrizes the decrease of detectable sources with distance due to the detection threshold (Kiraga & Paczyński 1994). For the main sequence stars, Kiraga & Paczyński (1994) and ZSR95 suggested $1 \leq \beta_s \leq 2$. For the clump giants, $\beta_s = 0$ is more appropriate as they are probably seen throughout the Galaxy. Note that $\langle \tau \rangle$ is generally a function of Galactic coordinates, but we ignore the angular variation inside a small field of view (less than one square degrees).

In all the following sections, we will use the Galacto-centric coordinate system (x, y, z) , with the Galactic centre at the origin, and the solar system at $(-R_0, 0, 0)$, where $R_0 = 8.5$ kpc is the distance to the Galactic centre. (X, Y, Z) are used to denote the coordinates along the three principal axes of the bar; X being the major axis of the bar. Since the tilt out of the Galactic plane is negligible (Dwek et al. 1995), the (X, Y, Z) coordinate system is simply related to (x, y, z) by a rotation of angle α in the $x - y$ plane. It is understood that only the absolute value of the angle, $|\alpha|$, is used.

Since the longest dimension of the bar, a , is still much smaller than the bar's distance from us, R_0 , we can make two simplifications to eq. (2) so that the calculations are tractable analytically:

(1) We set $n(D_s) = \rho(D_s)$, i.e., $\beta_s = 1$, so that the volume increase with distance just balances the decrease of detectable sources. This is a plausible assumption for the bulge main sequence stars, but probably underestimates the optical depth for the clump stars with $\beta_s = 0$ by an order of $(\frac{a}{R_0})$.

(2) We adopt a plane parallel approximation:

$$x_s \approx D_s - R_0, \quad x_l \approx D_d - R_0, \quad \frac{D_d}{D_s} \approx 1, \quad D = (D_s - D_d) \frac{D_d}{D_s} \approx x_s - x_l,$$

and the Galactic longitude and latitude of any bulge star

$$(l, b) \approx \left(\frac{y}{R_0}, \frac{z}{R_0} \right).$$

Here (y, z) are the coordinates where the line of sight intersects with $y - z$ plane at the center. x_s and x_l denote the x -coordinates of the source and the lens, which are assumed to be in the range of

$$-\infty < x_l \leq x_s < +\infty.$$

In making this simplification, we effectively set $-R_0 \rightarrow -\infty$, and $s_{max} \rightarrow \infty$. This is valid for lenses in the bar as long as the density of the bar falls off sufficiently fast or is truncated within a few kpc, which is the case for all our models. Note by letting $\frac{D_d}{D_s} = 1$ we overestimate D , and hence the optical depth, by an order of $(\frac{a}{R_0})$. The assumption also neglects the difference in distance between the positive and negative longitude sides.

With these simplifications, the optical depth for a source located at (x_s, y, z) is given by (cf. eq. 1)

$$\tau(x_s, y, z) = \frac{4\pi G}{c^2} \int_{-\infty}^{x_s} \rho(x_l, y, z) (x_s - x_l) dx_l. \quad (3)$$

while the average optical depth toward a field (y, z) is (cf. eq. 2)

$$\langle \tau(y, z) \rangle = \frac{\int_{-\infty}^{+\infty} dx_s \rho(x_s, y, z) \tau(x_s, y, z)}{\int_{-\infty}^{+\infty} dx_s \rho(x_s, y, z)}. \quad (4)$$

For the clump giants, the effects of our assumptions (1) and (2) on τ are in the opposite direction. Remarkably, numerical calculations find that these two effects cancel out, therefore, our analytical results based on eqs. (3) and (4) are accurate for the clump giants (cf. Fig. 3.) For the fainter main sequence stars eq. (4) overestimates the optical depth. But this can be easily corrected analytically to the first order of $\frac{a}{R_0}$ using eqs. (C21) and (C20) in

Appendix C. The corrected values are again in good agreement with numerical results. The analytical formulae, of course, have the significant advantage that they allow the dependence on the parameters to be studied explicitly (see §2.3.)

2.2 Analytical Results For a Gaussian Ellipsoidal Bar

Consider the optical depth of the Galactic bar with a Gaussian radial profile and an ellipsoidal shape, which is one of the models that Dwek et al. (1995) used to fit the COBE map.

The density of this model is given by

$$\rho(x, y, z) = \rho_0 \exp\left(-\frac{\lambda^2}{2}\right), \quad \rho_0 = \frac{M}{(2\pi)^{\frac{3}{2}}x_0y_0z_0}, \quad (5)$$

where

$$\lambda^2 = \left(\frac{X}{x_0}\right)^2 + \left(\frac{Y}{y_0}\right)^2 + \left(\frac{Z}{z_0}\right)^2, \quad (6)$$

M is the total mass of the bar, x_0, y_0, z_0 are the scale lengths along the three principal (X, Y, Z) axes of the bar and ρ_0 is the central density. X, Y, Z are related to x, y, z by a rotation of the bar angle α ,

$$X = x \cos \alpha - y \sin \alpha, \quad Y = x \sin \alpha + y \cos \alpha, \quad Z = z. \quad (7)$$

Substituting eq. (7) into eq. (6), one finds that

$$\lambda^2 = \left(\frac{x}{x_1}\right)^2 + \left(\frac{y}{y_1}\right)^2 + \left(\frac{z}{z_1}\right)^2 + 2\kappa xy, \quad (8)$$

where x_1, y_1 and z_1 are effectively the scale lengths along the x, y and z axes. Together with κ they are given by

$$\frac{1}{x_1^2} = \frac{\cos^2 \alpha}{x_0^2} + \frac{\sin^2 \alpha}{y_0^2}, \quad \frac{1}{y_1^2} = \frac{\sin^2 \alpha}{x_0^2} + \frac{\cos^2 \alpha}{y_0^2}, \quad \frac{1}{z_1^2} = \frac{1}{z_0^2}, \quad \kappa = \left(\frac{1}{y_0^2} - \frac{1}{x_0^2}\right) \sin \alpha \cos \alpha. \quad (9)$$

So for the Gaussian ellipsoidal bar, the optical depth for a source at the Galactic centre is (cf. eq. 3)

$$\tau(0, 0, 0) = \frac{4\pi G}{c^2} \int_{-\infty}^0 \rho_0 \exp\left(-\frac{x_l^2}{2x_1^2}\right)(-x_l) dx_l = \frac{4\pi G}{c^2} \rho_0 x_1^2. \quad (10)$$

The optical depth for a source on the minor axis at $(0, 0, z)$ is given by

$$\tau(0, 0, z) = \tau(0, 0, 0) \exp\left(-\frac{z^2}{2z_0^2}\right). \quad (11)$$

The optical depth for all sources along a line of sight passing the minor axis can be obtained from eq. (4)

$$\langle \tau(0, z) \rangle = \sqrt{2} \tau(0, 0, z) = \frac{4\pi G M}{c^2} \frac{1}{z_0} \frac{1}{\pi^{1/2}} I\left(\frac{y_0}{x_0}, \alpha\right) \exp\left(-\frac{z^2}{2z_0^2}\right), \quad (12)$$

where

$$I\left(\frac{y_0}{x_0}, \alpha\right) = \frac{1}{2\pi} \left[\left(\frac{y_0}{x_0} \cos^2 \alpha\right) + \left(\frac{x_0}{y_0} \sin^2 \alpha\right) \right]^{-1} = \frac{1}{\pi} \frac{(u + u^{-1})^{-1}}{\sin 2\alpha}, \quad u \equiv \frac{y_0/x_0}{\tan \alpha}. \quad (13)$$

Similarly we can obtain a microlensing optical depth map on the whole sky, i.e., on the whole $y - z$ plane:

$$\langle \tau(y, z) \rangle = \frac{4\pi G M}{c^2} \frac{1}{z_0} \frac{1}{\pi^{1/2}} I\left(\frac{y_0}{x_0}, \alpha\right) \exp\left(-\frac{y^2}{2y_1'^2} - \frac{z^2}{2z_0^2}\right), \quad y_1' \equiv \sqrt{x_0^2 \sin^2 \alpha + y_0^2 \cos^2 \alpha} \quad (14)$$

Note that for any field with the same z , the optical depth is the largest on the minor axis.

2.3 Analytical Results For a Family of Bar Models

The bar density is not uniquely constrained by the COBE map (Dwek et al. 1995). Models with various radial profiles and shapes can fit the data about equally well. In this section, we derive the optical depth for a general set of bar density models and show its dependence on the profile and shape of the bar.

Consider the following class of bar density models:

$$\rho(x, y, z) = \rho_0 f(\lambda), \quad f(\lambda) \equiv \left(1 + \frac{\lambda^n}{\beta - 3}\right)^{-\frac{\beta}{n}}, \quad (15)$$

where the central density ρ_0 can be expressed in terms of the total mass of the bar, M , and is given in eq. (A1) in the Appendix A. The effective dimensionless radius parameter λ is given by

$$\lambda^n = \left[\left| \frac{X}{x_0} \right|^k + \left| \frac{Y}{y_0} \right|^k \right]^{\frac{n}{k}} + \left| \frac{Z}{z_0} \right|^n. \quad (16)$$

The parameters n and k determine the shape of the bar: k specifies the shape of the bar in the $X - Y$ plane while n specifies the shape in the $Y - Z$ and $X - Z$ planes. The parameter β describes the radial profile of the bar. When $\beta > 0$, the density falls off like a power-law with slope $(-\beta)$ at large radius. When $\beta \leq 0$, the model describes a truncated finite bar confined within $\lambda \leq |\beta - 3|^{\frac{1}{n}}$. When $\beta \rightarrow \infty$, one obtains an exponential or Gaussian density profile for $n = 1$ or $n = 2$. The Gaussian ellipsoidal model studied in the previous section corresponds to a special case with $(\beta, n, k) = (\infty, 2, 2)$. A homogeneous rectangular bar corresponds to a model with $(\beta, n, k) = (0, \infty, \infty)$; analytical results for this special case are given in the Appendix B.

This family embodies the more interesting cases of bar models[†] and can simulate a great

[†] models with $0 < \beta \leq 3$ correspond to flaring bars with their densities increase with radius, and will not be considered further.

diversity of shapes and radial profiles. The range of shapes and profiles are demonstrated by a few examples in Fig. 1a and 1b.

Similar to the Gaussian ellipsoidal bar model, one can show that for this family the optical depth at any minor axis field depends on z as:

$$\langle \tau(0, z) \rangle = \frac{4\pi G M}{c^2 z_0} \xi_0(\beta, n) H(k, \frac{y_0}{x_0}, \alpha) \left[1 + \frac{1}{\beta - 3} \left(\frac{|z|}{z_0} \right)^n \right]^{-\frac{\beta-2}{n}}, \quad (17)$$

where

$$H(k, \frac{y_0}{x_0}, \alpha) = \frac{1}{K(k)} \left[\left(\frac{y_0}{x_0} \cos^2 \alpha \right)^{\frac{k}{2}} + \left(\frac{x_0}{y_0} \sin^2 \alpha \right)^{\frac{k}{2}} \right]^{-k/2} = \frac{1}{K(k)} \frac{2 \left(u^{\frac{k}{2}} + u^{-\frac{k}{2}} \right)^{-2/k}}{\sin 2\alpha}, \quad (18)$$

$\xi_0(\beta, n) \approx 0.6 \pm 0.15$ is a slow varying function of β and n , u is as defined in eq. (13), $K(k) = 4k^{-1}B(k^{-1}, k^{-1})$, and B is the complete Beta-function. For clarity, we have deferred the somewhat lengthy definition of ξ_0 (together with several useful approximations) until Appendix A. Eq. (17) reduces to eq. (12) for a Gaussian ellipsoidal bar when $(\beta, n, k) = (\infty, 2, 2)$, with $\xi_0 = \pi^{-1/2}$, $H(2, y_0/x_0, \alpha) = I(y_0/x_0, \alpha)$.

For ellipsoidal models with $n = k = 2$, an analogous microlensing map as eq. (14) can be derived. We find

$$\langle \tau(y, z) \rangle = \langle \tau(0, 0) \rangle \left[1 + \frac{1}{\beta - 3} \left(\frac{y^2}{y_1'^2} + \frac{z^2}{z_0^2} \right) \right]^{-\frac{\beta-2}{2}}, \quad \text{if } n = k = 2, \quad (19)$$

where y_1' is given by eqs. (14) and (9). Along the line with a constant z , the optical depth is the largest on the minor axis $y = 0$.

Eq. (17) is our main analytical result. In the rest of this section, we will study the dependence of the optical depth on the parameters.

2.3.1 Dependence on Radial Density Profile and Latitude

(1) The optical depth due to the bar lenses, τ , is proportional to the total bar mass M , as expected.

(2) τ falls off on the minor axis as $\left[\frac{\rho(z)}{\rho(0)} \right]^{1-\frac{2}{\beta}}$ (cf. eqs. 16 and 17). When $\beta > 3$, the model is a power-law with a finite mass, τ falls off slower than the density. When $\beta \leq 0$, the model is truncated at a finite size, τ falls off faster than the density. When $\beta \rightarrow \infty$, τ falls off as the density.

(3) For a fixed field z kpc above the plane, τ first increases and then decreases with the vertical scale length z_0 , and τ is maximized when the scale height $z_0 = z$. This is because

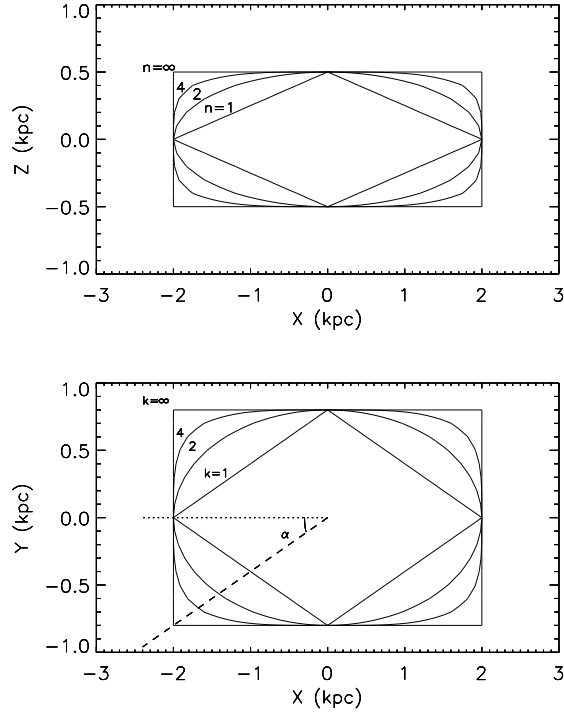
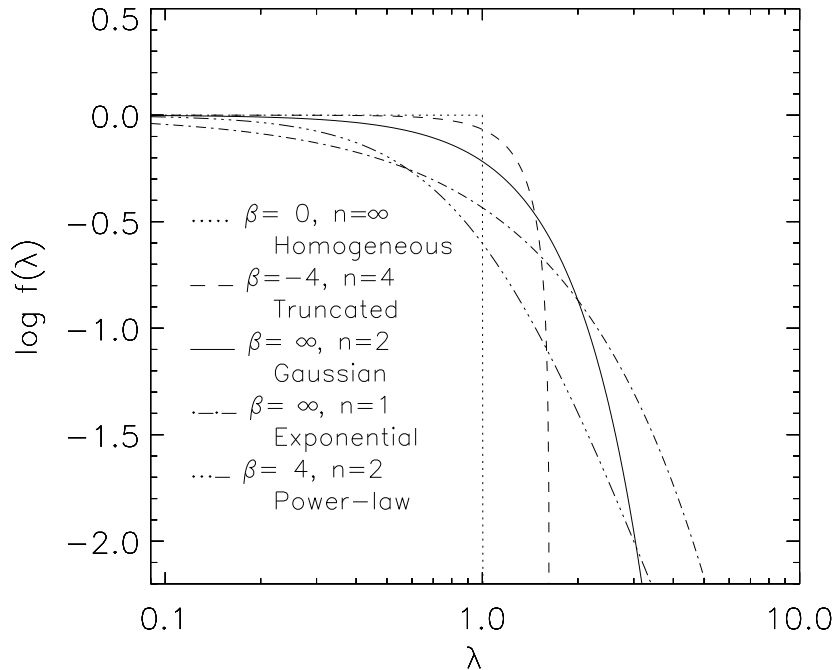


Figure 1. (a) Some examples of geometrical shapes are shown for the family of bar models as described by eqs. (15) and (16). For illustration we used a bar with axis scale lengths $x_0 : y_0 : z_0 = 2 : 0.8 : 0.5$ (kpc), similar to the scale lengths of the COBE constrained GE model (cf. Table 1.) The shapes in the X-Y plane are determined by k while the shapes in the X-Z (also Y-Z but not shown) plane are determined by n . The shape of the bar evolves from being diamond, ellipsoidal, boxy to rectangular when k or n are increased in the sequence of 1, 2, 4, and ∞ . The dashed line indicates our line of sight to the center, which makes an angle α with the major (X) axis of the bar. Observationally, $\alpha \sim 10^\circ - 45^\circ$ with the near end of the bar in the first Galactic quadrant.



(b) Some examples of radial profiles are shown for the same family of bar models. The density profiles are described by two parameters n and β in the radial coordinates expressed by λ (cf. eqs. 15 and 16). All the density profiles are normalized to the central density.

increasing the scale height leads to both a shallower density gradient and a smaller central density. To obtain the maximum optical depth, we note that in eq. (17) the factor

$$\frac{M}{z_0} \left[1 + \frac{1}{\beta - 3} \left(\frac{z}{z_0} \right)^n \right]^{-\frac{\beta-2}{n}} \leq \frac{M}{z} \left(\frac{\beta - 2}{\beta - 3} \right)^{-\frac{\beta-2}{n}}. \quad (20)$$

The equality sign indicates the maximum and is reached when $z_0 = z$ irrespective of β .

2.3.2 Dependence on Bar Angle and Shape

Not surprisingly, τ depends on some combinations of the angle, axis ratio and the shape of the bar, more specifically:

(4) For fixed axis ratio and shape, τ is largest when the bar points toward us, i.e., when $\alpha = 0$. In this case, $\tau \propto H(k, \frac{y_0}{x_0}, 0) \propto \frac{x_0}{y_0}$ (cf. eqs. 17 and 18).

(5) For a fixed angle $\alpha < 45^\circ$, gradually squashing an oblate bulge to make it increasingly elliptical in the $x - y$ plane leads to a monotonic increase in the optical depth until $\frac{y_0}{x_0} \leq \tan(\alpha)$. For $\alpha > 45^\circ$, the optical depth always decreases when y_0/x_0 changes from one to zero. τ has a maximum at $u = 1$ (cf. eq. 18), i.e., at $\frac{y_0}{x_0} = \tan \alpha$. This is graphically shown in the upper panel of Fig. 2 for $k = 2$ models. The turn-over for very small axis ratio can be intuitively understood as a needle-shaped bar pointing sideways has zero depth to place the lens and the source along the line of sight, hence zero optical depth. Mathematically, τ is proportional to H (cf. eq. 17), and

$$H(k, \frac{y_0}{x_0}, \alpha) = \frac{2}{K(k)} \frac{\left(u^{\frac{k}{2}} + u^{-\frac{k}{2}} \right)^{-2/k}}{\sin 2\alpha} \leq \frac{2}{K(k)} \frac{2^{-\frac{2}{k}}}{\sin 2\alpha}. \quad (21)$$

So τ and H are maximized at $u = 1$ irrespective of k .

(6) The maximum gain in optical depth of an elliptical ($k = 2$) bar vs an oblate bulge is given by

$$\frac{\tau_{\text{bar}}}{\tau_{\text{bulge}}} \leq \frac{1}{\sin 2\alpha}, \quad (22)$$

where the maximum is at $\frac{y_0}{x_0} = \tan \alpha$. For example a bar with $\alpha = \arctan^{-1} \frac{y_0}{x_0} = 15^\circ$ gains by a factor of 2. But for $\alpha \geq 45^\circ$ the oblate model predicts higher optical depth than bar models.

(7) Other things being equal, τ is a slow varying function of n . The ratios for $n = 1, 2, 4$ (diamond, ellipsoidal, boxy) for $\beta \rightarrow +\infty$ are about 1.3 : 1 : 0.95, while for $\beta = 4$ the ratios are 1.68 : 1 : 0.82.

(8) Similarly, for fixed axis ratio and angle, varying k , τ changes by less than a factor of

2 (see Fig. 2, lower panel). The ratios of the optical depth τ for the diamond shape ($k = 1$) to that for an ellipsoidal shape ($k = 2$) are 1.57, 1, and 0.79 at $u = \frac{y_0/x_0}{\tan(\alpha)} = 0, 0.31,$ and 1 respectively. The variation is the same for $u > 1$ due to the symmetry between u and u^{-1} (cf. eq. [17]).

(9) Of the whole class of models with different central densities and shapes, the optical depth is the largest for a homogeneous rectangular (HR) bar. The maximum optical depth is reached when $\alpha = \tan^{-1}\left(\frac{y_0}{x_0}\right)$, i.e., when the line of sight coincides with the diagonal line of the homogeneous rectangular bar. The microlensing map of this model is given by equations in Appendix B. A comparison of the homogeneous rectangular (HR) model with models of other shapes is in § 3.5.

3 APPLICATION TO THE GALACTIC BAR

The formalism we have developed can be applied to any edge-on bar. In this section, we will concentrate on the Galactic bar, where most microlensing events are observed (Alcock 1995b; Udalski et al. 1994; Alard et al. 1995). As the optical depth is a function of the bar parameters such as the total mass, bar angle and axial scale lengths, we therefore first outline the uncertainties in these parameters before we proceed to estimate the optical depth.

3.1 Uncertainties in the Bar Parameters

Dwek et al. (1995) carried out a systematic study of the bar parameters by fitting the COBE map. A few models can fit the data well, i.e., the parameters are not well constrained. For non-axisymmetric models, the bar angle lies $10^\circ \lesssim \alpha \lesssim 45^\circ$, and the axis ratio $y_0/x_0 = 0.15 - 0.5$, and the vertical scale height $z_0 = 200 - 500$ pc. In Table I, we have listed four models from Dwek et al. (1995) that can be described by our parametrization in eqs. (15) and (16). Except for the power-law exponential model, the errorbars for the parameters are quite small (cf. Table 1), while the variations from model to model are quite large. For each model, we will take the best-fit (central) parameter values in the table and evaluate the optical depth. We do not attempt to do a full error analysis due to the correlation of errors between parameters. Out of the four models, the Gaussian ellipsoidal model provides the best fit to the COBE map, while the exponential diamond (ED), oblate bulge (OB) and power-law ellipsoidal (PE) profiles become progressively less satisfactory. Note that the oblate bulge model is an axisymmetric model. Two additional models are listed in Table 1, one being

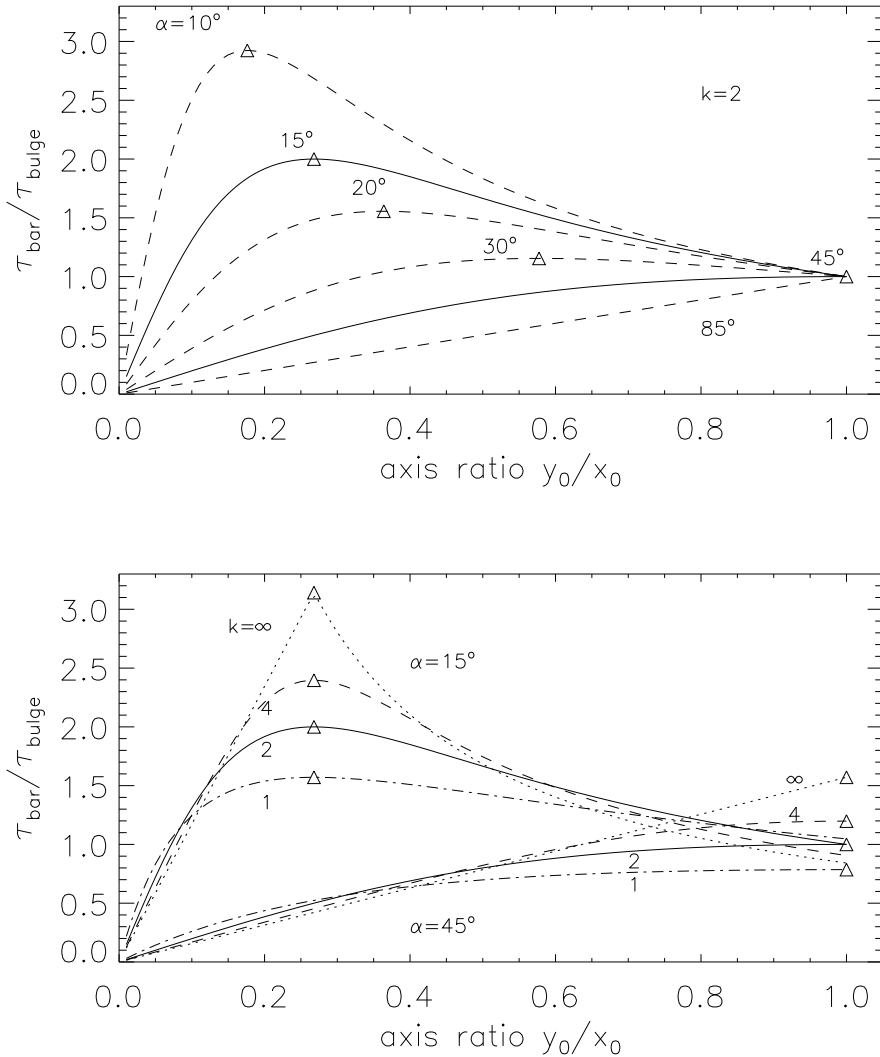


Figure 2. shows the ratio of optical depths of a bar vs an oblate bulge as a function of the bar angle and shape. The upper panel shows that for an elliptical bar ($k = 2$), the optical depth peaks at an axis ratio $\frac{y_0}{x_0} = \tan(\alpha)$ if the bar angle $\alpha \leq 45^\circ$. For $\alpha \geq 45^\circ$, the optical depths increases monotonically with the axis ratio y_0/x_0 , and is always smaller than that of an oblate bulge model. Note an elliptical bar becomes an oblate bulge at $\frac{y_0}{x_0} = 1$. For a bar angle $\alpha = 15^\circ$, the lower panel shows that an elliptical bar gives a larger peak (maximum) optical depth than that for a diamond shaped bar ($k = 1$), but less than those for a boxy bar ($k = 4$), and a homogeneous bar. The positions of the maximum optical depths are indicated by triangles. They always occur at the axis ratio $\frac{y_0}{x_0} = \tan(\alpha) = 0.27$ for $\alpha = 15^\circ$.

a truncated boxy (TB) bar model, and the last one a homogeneous rectangular (HR) bar. These models are interesting since extragalactic bars often have a flat density profile and a sharp truncation near corotation (Sellwood & Wilkinson 1993). For these two models, the bar parameters are not available and we only consider their optimal lensing configurations. These six models should offer a broad survey of the uncertainty in the optical depth.

The mass of the Galactic bar cannot be derived directly from the COBE map. However, it can be obtained by fitting either the gas rotation curve or the stellar velocity dispersions.

Table 1. Parameters for Six Galactic Bar Models

Model	OB (G0)	GE (G1)	ED (E1)	PE (P3)	TB	HR
Description	Oblate	Gaussian, Ellipsoidal	Exponential, Diamond	Power-Law, Ellipsoidal	Truncated, Boxy	Homogeneous, Rectangular
(β, n, k)	$(\infty, 2, 2)$	$(\infty, 2, 2)$	$(\infty, 1, 1)$	$(4, 2, 2)$	$(-4, 4, 2)$	$(0, \infty, \infty)$
$\alpha(^{\circ})$	—	11 ± 2.4	24.4 ± 6.7	45.4 ± 33.3	—	—
x_0 (kpc)	0.91 ± 0.01	2.08 ± 0.06	1.64 ± 0.06	0.90 ± 0.2	—	—
y_0 (kpc)	0.91 ± 0.01	0.75 ± 0.01	0.61 ± 0.11	0.23 ± 0.98	—	—
z_0 (kpc)	0.51 ± 0.01	0.45 ± 0.02	0.31 ± 0.01	0.28 ± 0.04	—	—
$\xi_0(\beta, n)$	0.564	0.564	0.75	0.477	0.554	0.667
$\xi_4(\beta, n)$	1.772	1.772	2.55	2.094	1.376	1
$H(k, \frac{y_0}{x_0}, \alpha)$	0.159	0.354	0.165	0.08	—	—
$\langle \tau_{-6}(0, 0) \rangle$	2.9	7.3	6.5	2.2	—	—
$\langle \tau_{-6}(0, -2^{\circ}) \rangle$	2.4	5.8	2.5	1.1	—	—
$\langle \tau_{-6}(0, -4^{\circ}) \rangle$	1.5	3.1	0.94	0.41	—	—
$\langle \tau_{-6}(0, -6^{\circ}) \rangle$	0.64	1.1	0.38	0.20	—	—

Six models for a very massive ($M = 2.8 \times 10^{10} M_{\odot}$) Galactic bar. The radial profiles and geometrical shapes of the models are described in the second and third rows. The initials of these descriptions in the first row are used to label the curves in the figures. The first four models are the same as the G0, G1, E1, and P3 models in Dwek et al. (1995). (β, n, k) are parameters that describe the shape of the bar (cf. eq. 16). α is the angle between the direction to the Galactic centre and the major (X) axis of the bar. x_0, y_0, z_0 are the scale lengths of the three principal axes of the bar. The parameters for the first four models are taken from Table 1 in Dwek et al. (1995) at $2.2 \mu\text{m}$ with $R_{max} = \infty$. $\xi_0(\beta, n)$, $\xi_4(\beta, n)$ and $H(k, y_0/x_0, \alpha)$ are functions of β, n, k, α and y_0/x_0 . These are used in eqs. (17) and (C20) to evaluate the optical depth. The last four rows list the predicted optical depths due to lenses in the bar at four fields; the values would scale linearly for other choice of the bar mass M (eq. 25 gives the range of M).

Generally axisymmetric models such as the Kent's (1992) oblate rotator model (cf. the oblate model in Table 1) fail to match the gas rotation curve either at $R \approx 0.5$ kpc or at $R \approx 3$ kpc. Triaxial models with and without pattern rotation can be made consistent with the gas rotation curve. A rough limit on the mass of the bar can be set as follows:

If the bar is contained within a corotation radius of $R_{\text{cor}} \approx 2.4$ kpc (Binney et al. 1991), then the enclosed dynamical mass, $M_d + M$, satisfies

$$\eta \frac{G(M_d + M)}{R_{\text{cor}}} = V_c^2(R_{\text{cor}}), \quad (23)$$

where M_d is the mass contributed by the disk within R_{cor} , and $V_c(R_{\text{cor}}) \approx 195 \text{ km s}^{-1}$ is the circular velocity at the corotation radius. The parameter η is a factor that describes the enhanced gravity of a flattened or barred system relative to a spherical system. Since $\eta \geq 1$ and $M_d \sim (10\% - 20\%)M > 0$, we derive a loose upper bound for the bar mass,

$$M \lesssim 2.2 \times 10^{10} M_{\odot} \quad (24)$$

by setting $\eta = 1$ and $M_d = 0$.

More detailed gas modelling that matches the non-self-crossing closed orbits with the gas terminal velocity gives a very similar value. Assuming different pattern speeds, viewing angles, and bar density profiles, several authors find $M = (2.2 \pm 0.2) \times 10^{10} M_{\odot}$ (Gerhard & Vietri 1986; Binney et al. 1991; ZRS96)

The mass obtained by different authors using the stellar velocity dispersions of bulge

stars has a larger scatter. This is mainly due to different levels of sophistication in the dynamical models. The simple oblate rotator model by Kent (1991) predicts a low value, $M = 1.8 \times 10^{10} M_{\odot}$ based on the pre-COBE data. The detailed steady state bar model of Zhao (1996), which fits the COBE map with a positive definite distribution function, gives $M = (2.2 \pm 0.2) \times 10^{10} M_{\odot}$. Straightforward but less certain application of the Virial theorem predicts between $M = 1.8 \times 10^{10} M_{\odot}$ with no pattern rotation of the bar (Han & Gould 1995), and $M = 2.8 \times 10^{10} M_{\odot}$ with a big pattern rotation (Blum 1995).

To summarize, the predicted mass of the bar by different authors is in the range of

$$1.8 \times 10^{10} M_{\odot} \leq M \leq 2.8 \times 10^{10} M_{\odot}. \quad (25)$$

3.2 Optical Depth of Disk Lenses

To compare our bar models with observations, the contribution from the disk lenses must be added. It is well known that a standard disk model predicts $\tau_{\text{disk},-6} \approx 0.66$ at Baade window, too small to explain the observed high optical depth. However, our predictions for disk lenses are still uncertain due to lack of constraints of faint disk sources at several kpc from the Galactic center. ZSR95 find that the optical depth of the disk is in the range of $0.37 - 0.87$ for Baade window by extrapolating the local disk density with a double-exponential disk model with different disk scale length, scale height and local density normalization. The lower end is from a disk with a central hole as suggested by Paczyński et al (1994b) based on color-magnitude diagrams of OGLE stars. A much higher disk optical depth ($\tau_{\text{disk},-6} = 2$) would require the disk to make up most of the rotation curve, which appears to be in conflict with the lack of faint stars or brown dwarfs in the solar neighbourhood (Gould, Bahcall, & Flynn 1996). As the effect of the disk is small, in this paper, we will simply adopt

$$\tau_{\text{disk},-6} \approx 0.35 - 1, \quad (26)$$

and completely ignore its z dependence. This range is indicated by two thick horizontal bars at the bottom left in Figures 3–6.

3.3 Optical Depth of the COBE Bar: Red Clump Sources

Having discussed the possible ranges of the bar parameters and the disk contribution, we can now investigate the optical depth of the COBE bar. For bright red clump giants in the bulge, we can apply eq. (17), which we rewrite as

$$\langle \tau_{-6}(0, z) \rangle = 2.1 \frac{M}{2 \times 10^{10} M_{\odot}} \frac{0.5 \text{kpc}}{z_0} \frac{\xi_0(\beta, n, k)}{0.564} \frac{H(k, \frac{y_0}{x_0}, \alpha)}{0.159} \left[1 + \frac{1}{\beta - 3} \left(\frac{|z|}{z_0} \right)^n \right]^{-\frac{\beta-2}{n}}, \quad (27)$$

where we have normalized the quantities $\xi_0(\beta, n, k)$ and $H(k, y_0/x_0, \alpha)$ to the values for an oblate bulge, i.e., for $y_0/x_0 = 1$ and $n = k = 2$.

Table 1 gives the optical depths for four latitudes along the minor axis for the four models taken from Dwek et al. (1995). The field at $(0^\circ, -4^\circ)$ is close to Baade window. The values are for $M = 2.8 \times 10^{10} M_{\odot}$, at the upper end of eq. (25), but this can be scaled linearly for other M . There are two things worth pointing out: first, at the same field the optical depths of different models differ by a factor 3–5; second, the optical depth drops with latitude for each model. From the Galactic center to Baade window, the decrease is about a factor of 6 for the exponential diamond (ED) and the power-law ellipsoidal (PE) models, but only about a factor of 2–3 for other models. The fast decrease of the exponential diamond and power-law ellipsoidal models are obviously due to their steep density profiles (cf. Fig.1b and Table 1).

These points are further illustrated in Fig. 3, where we have plotted the variation of the optical depth of the bar along the minor axis. The black dots with 2σ errorbars are the inferred optical depths for the low latitude and high latitude clump giants (Alcock et al. 1995b). Notice the data is suggestive of a decrease in the optical depth with latitude.

Now let us examine Fig. 3 more closely. We notice that the errorbars are very large, which is hardly surprising because the two subsamples have only 10 and 3 events, respectively! Still, out of the four models, only the Gaussian ellipsoidal (GE) model can produce an optical depth as high as $\tau_{-6} = 6$. This is achieved only when the bar is very massive, with $M = 2.8 \times 10^{10} M_{\odot}$ and with a large disk contribution, $\tau_{\text{disk}, -6} = 1$. For the same condition, the oblate bulge and exponential diamond models are only at the 2σ lower limit. The power-law ellipsoidal model produces an optical depth simply too small to be consistent with observation. This is mainly due to the large bar angle, $\alpha \approx 45^\circ$, rendering a very inefficient lensing configuration.

3.4 Optical Depth of the COBE Bar: Main Sequence Sources

We can carry out a similar analysis for the main sequence stars. The analytical formulae that apply to these stars are given in eqs. (C20) and (C21). But in Fig. 4, we only show

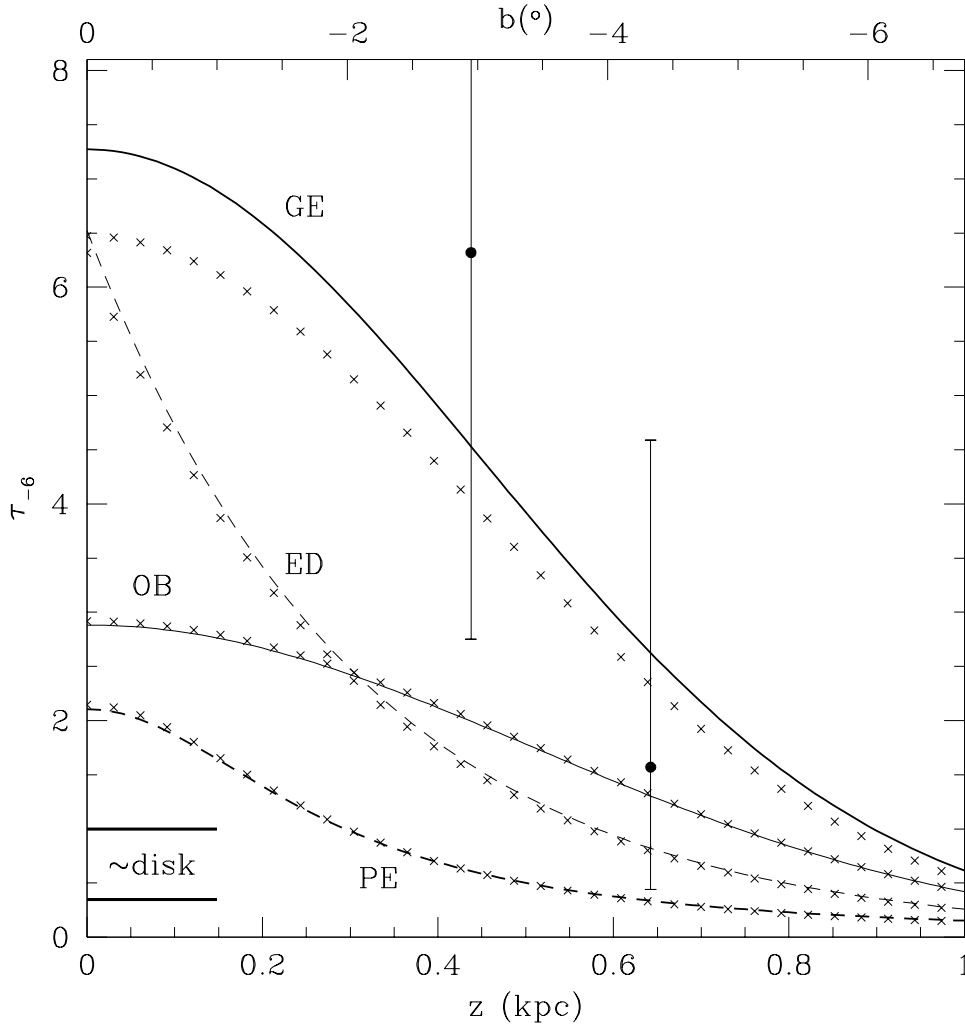


Figure 3. Optical depths on the z (minor) axis are shown for four COBE constrained bar models (columns 2 to 5 in Table 1) for clump sources. The z coordinate and latitude are shown at the bottom and top axes respectively. The abbreviations for the models are given in Table 1. All the optical depths are for a very massive bar with $M = 2.8 \times 10^{10} M_{\odot}$, but can be scaled linearly for other masses (the range is given in eq. 25). The approximate range of the optical depth contributed by the disk are indicated with two short thick lines at the bottom left. The total optical can be calculated by first linearly scaling the plotted values for different M and then add the disk contribution. The two black dots are the optical depths observed for the low and high latitude clump giants (Alcock et al. 1995b). The 2σ errorbars are also plotted. The crosses indicate full numerical calculations for each model.

the numerical results from eq. (2). Each shaded region corresponds to one model, with the upper and lower curves for $\beta_s = 1$ and $\beta_s = 2$ respectively.

Quite strikingly the optical depth decreases with increasing β_s , which may explain the smaller optical depth for main sequence stars $\beta_s > 0$ in the MACHO sample than for the clump giants $\beta_s = 0$. For the Gaussian ellipsoidal model, the optical depth drops by a factor of 2 from $\beta_s = 0$ to $\beta_s = 2$, while the power-law ellipsoidal model is almost unchanged. For the other two models, the decrease is about (20-50)%. Increasing β_s effectively moves

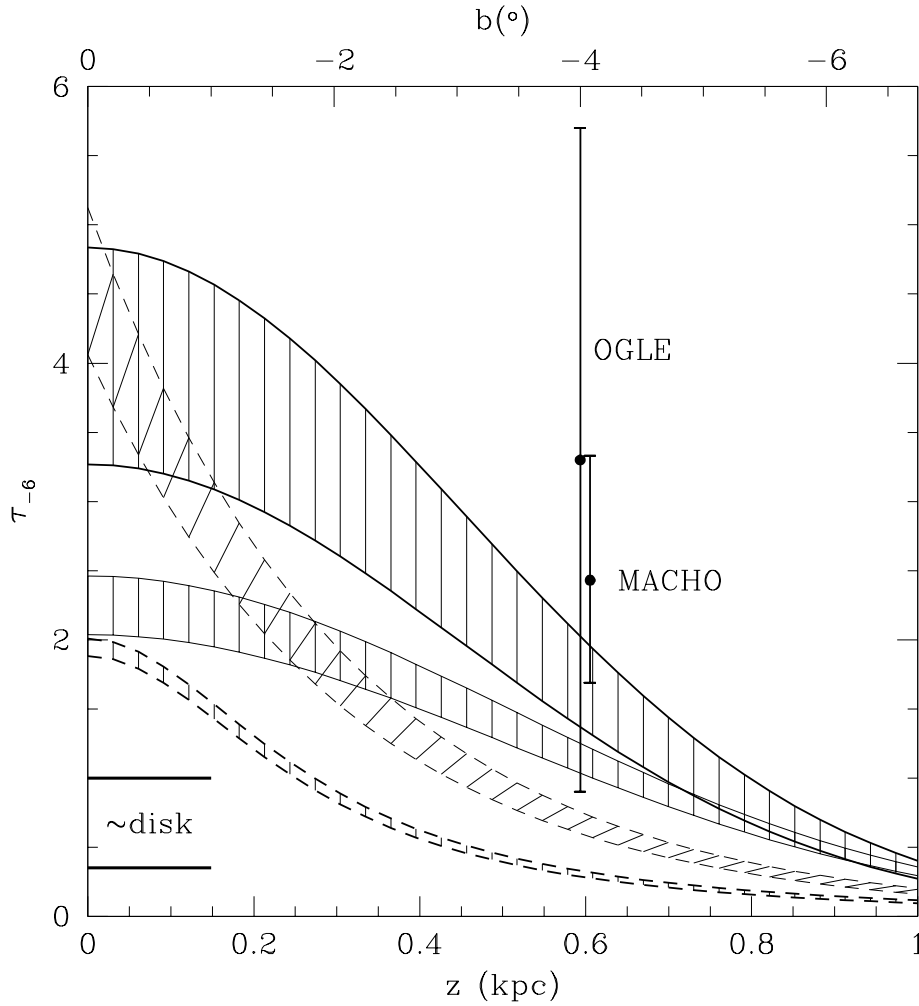


Figure 4. Similar to Fig. 3, but for minor axis optical depth of four COBE models with source being bulge main sequence sources. Each shaded region corresponds to one model, with the top curve for $\beta_s = 1$ and the lower curve for $\beta_s = 2$. Again, a very massive bar with $M = 2.8 \times 10^{10} M_\odot$ is used. The optical depths for the full MACHO and OGLE samples are shown together with their 2σ errorbars.

the average source closer to us and reduces the optical depth by a factor proportional to $\frac{x_1}{R_0} \beta_s$, where x_1 is the scale length in the line of sight (cf. eq.9). The Gaussian ellipsoidal model has the largest major axis length and smallest angle α , hence the largest x_1 , the reduction for this model is therefore the strongest. The decrease of τ for intrinsically faint sources can potentially provide interesting limits on the source luminosity function if the bar is sufficiently extended.

In the same figure, the optical depths from 41 MACHO events and 9 OGLE events are shown with their 2σ errorbars. With a bar mass of $M = 2.8 \times 10^{10} M_\odot$ and a disk contribution of 10^{-6} , only the Gaussian ellipsoidal and exponential diamond models are within the 2σ

errorbars of the MACHO sample. For the diamond exponential and power-law ellipsoidal models, the optical depths are too small even if we adopt a large bar mass and substantial disk contribution.

3.5 Optimal Lensing Configuration of the Bar

We have so far studied the COBE constrained bar models. Three out of the four models have difficulties in reproducing the observed high optimal depth. It is therefore interesting to examine whether these bar models – disregarding the COBE constraints – can produce the high optical depth at all. In other words, we want to know the maximum optical depth for each model by adopting the optical lensing parameters. For this exercise, we will concentrate on the clump giants as these are less prone to systematic effects such as blending and also because they appear to have larger optical depths. As the observed fields of MACHO and OGLE are centred near Baade window, we choose to maximize the optical depth at this window for each model.

For each of the six sets of (β, n, k) in Table 1, the optical depth at Baade window depends linearly on the total mass and on some combinations of the angle α , the axis ratio y_0/x_0 , and the vertical scale height z_0 . For the Baade window, the most favorable lensing configuration is when the vertical scale height $z_0 = z_{BW} \approx 590$ pc (see the discussion at the end of §2.3.1), and the axis ratio $y_0/x_0 = \tan \alpha$.

In Fig. 5, we plot the optical depth for the above six bar models each at its most favorable configuration ($z_0 = z_{BW}$ and $y_0/x_0 = \tan \alpha$) as a function of the bar angle α . Clearly for each model the optical depth drops quickly when α is increased from 0° to 20° , after which the curves become nearly flat. This is simply due to the factor $1/\sin(2\alpha)$ in $H(k, y_0/x_0, \alpha)$ (cf. eq. 18).

The six models in Table 1 have different radial profiles and boxyness due to their different (β, n, k) . Fig. 5 shows that the boxy bars with a flat density profile have an interesting signature of in optical depth. For any given bar angle the optical depth is the largest for the homogeneous rectangular bar. Intuitively this can be understood as follows. A large optical depth to the bulge requires putting as many lenses as possible at positions as distant as possible from the source. A model with a flat density profile in the line of sight places more lenses at the near side and more sources at the far side than a model with a step density profile, hence a model with a flat profile is a more favorable lensing configuration.

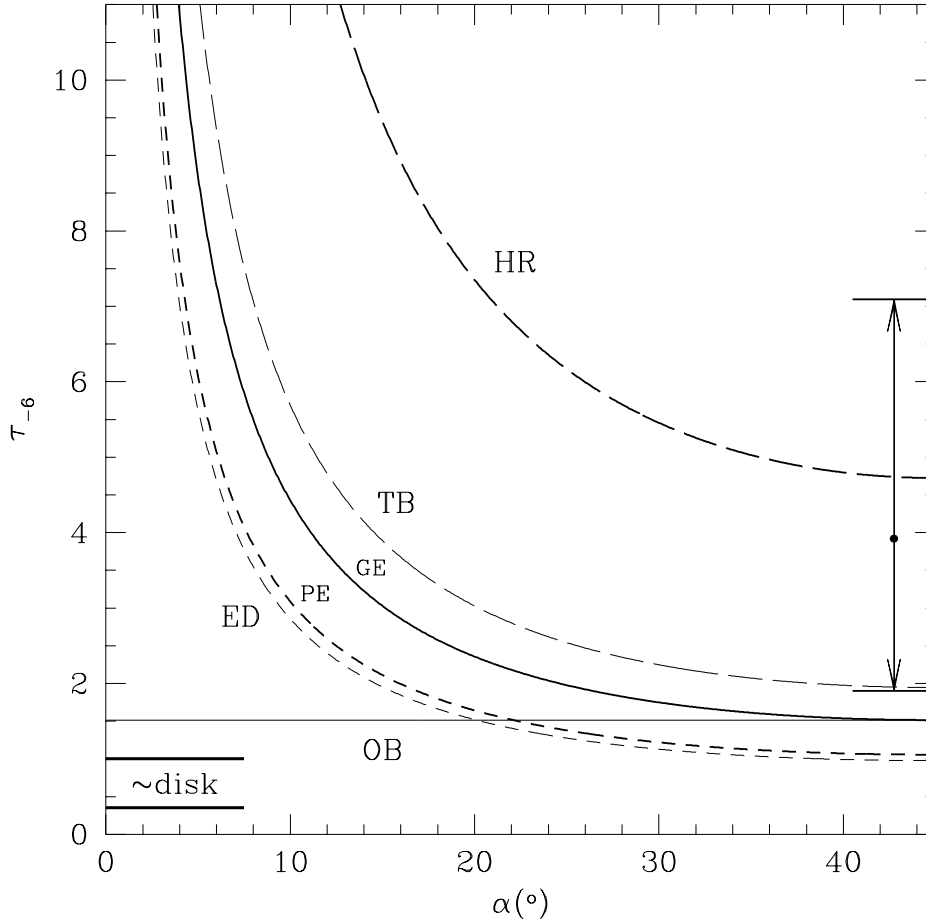


Figure 5. Optimal optical depths at Baade window are shown as a function of the bar angle α , for a very massive bar $M = 2.8 \times 10^{10} M_{\odot}$. To achieve the optimal optical depth, the vertical scale height is fixed to be $z_0 = 590$ pc, and the axis ratio $y_0/x_0 = \tan \alpha$. The abbreviations for the models are listed in Table 1. The observed range of optical depth for the clump giants (Alcock et al. 1995b) is shown by two horizontal bars with arrows with the black dot indicating the central value. The approximate optical depth contributed by the disk lenses are plotted with two short thick lines at the bottom left. The total optical depth can be calculated by first scaling the plotted values linearly for different M and then adding the disk contribution.

In addition, for a homogeneous bar the number of lenses does not decrease as one moves up on the minor axis before reaching the boundary. A rectangular bar furthermore stretches the distance between the lens and source even more as it has the longest contributing line of sight. A diamond shaped model, on the contrary, has the shortest contributing line of sight. These points become clear by comparing the length of segments of the dashed line intercepting the rectangular contour and the diamond contour in the bottom panel of Fig. 1a. Using the same argument, one can understand why the truncated boxy model (TB model in Fig. 5) also has a large optical depth.

This figure also points out the promise of the microlensing technique. If the present observed mean value of the optical depth is the true value, we see from Fig. 5 that all the bar models must have angle within 20° except the extreme homogeneous rectangular (HR) model. Unfortunately, if the lower 2σ bound of the optical depth is true, and if one adopts a massive bar and a large disk contribution ($\tau_{\text{disk},-6} = 1$), then the current sample provides little constraint on the bar angle. The situation could be improved significantly with a factor of four increase in the sample size; the errorbar will be reduced by a factor of two. If the optical depth $\tau_{-6} \geq 3.9$ were confirmed, then the most plausible models would be a $M \geq 2 \times 10^{10} M_\odot$ truncated boxy (TB) bar with an angle $\alpha = 10^\circ - 20^\circ$, and axis ratio $\frac{z_0}{x_0} \leq \frac{y_0}{x_0} \approx \tan(\alpha)$ plus a modest contribution of disk lenses. The optical depth $\tau_{-6} \sim 12$ at the high 2σ end of the MACHO clump giant sample is likely unphysical since it would argue for one of the following: (a) an extremely elongated bar with $\frac{y_0}{x_0} = \tan(\alpha) \approx 0.05$ and the line of sight almost coincides with the major axis of the bar: $\alpha = 2^\circ - 5^\circ$; (b) an very elongated homogeneous rectangular bar with $\alpha \approx 10^\circ$; (c) a drastically different picture of the mass distribution in the Galaxy. The first two possibilities are probably ruled out by the COBE map, while the third one will have a host of difficulties with the gas and stellar kinematics.

In Fig. 5, we have taken α as a complete free parameter, and the axis ratio is set such as to achieve the maximum optical depth. Now we want to examine possible constraint for the axis ratio. To do this, we take $\alpha = 10^\circ$, i.e., at the lower end of the inferred bar angle (cf. Table 1), keeping $z = z_0$, and study the variation of optical depth with the axis ratio. The results are plotted in Fig. 6. Big optical depth would imply that the axis ratio $\frac{y_0}{x_0}$ is close to the optimal value $\tan(\alpha)$. Unfortunately the current data gives only a rather weak limit at 95% confidence level. However, if we take the mean value of the MACHO experiment and a disk contribution of 10^{-6} , we can place non-trivial constraints on the axis ratio. For example, for the GE model, we will limit the axis ratio to be $0.05 < y_0/x_0 < 0.5$; the observed value 0.35 for GE model (cf. Table 1) is within this limit. More definite limits are only possible when the sample size is increased a few times and the errorbars are reduced.

4 DISCUSSION

We have evaluated the optical depths for a family of bar models. The analytical formulae developed are applicable to both the bulge clump giants and the main sequence stars. We

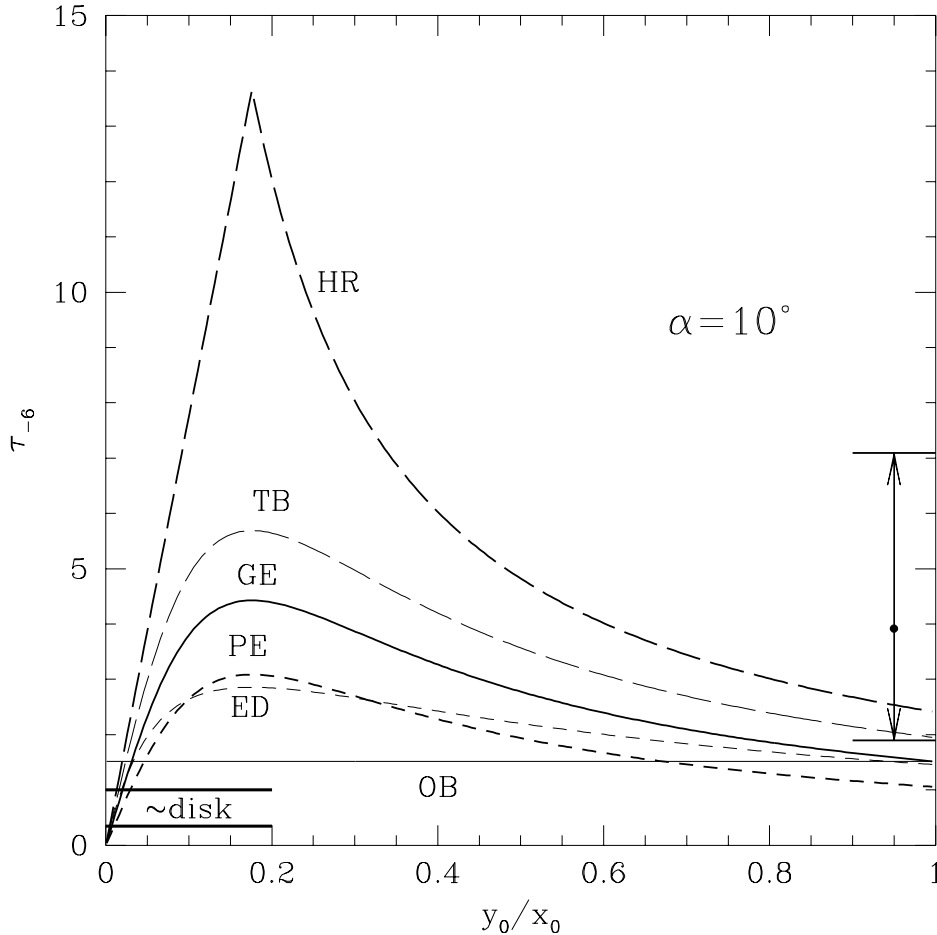


Figure 6. Optical depths at Baade window are shown as a function of the axis ratio $\frac{y_0}{x_0}$ for a very massive bar, $M = 2.8 \times 10^{10} M_\odot$, with a fixed angle $\alpha = 10^\circ$. The vertical scale height for each model is set to be $z_0 = 590$ pc. The abbreviations for the models are listed in Table 1. $M = 2.8 \times 10^{10} M_\odot$. The observed optical depth for all the clump giants by Alcock et al. (1995b) is shown by two horizontal bars with arrows with the central value indicated by a black dot. The approximate range of the optical depth contributed by the disk lenses are indicated by two short thick lines at the bottom left. The total optical can be calculated by first scaling the plotted optical depth linearly for different M and then adding the disk contribution.

have studied the dependence of the optical depth on the bar parameters. With about 50 microlensing events, we have demonstrated that microlensing already provides interesting constraints on the bar models. For example, the COBE constrained power-law ellipsoidal (PE) model produces an optical depth just too small to be consistent with the observed optical depths, primarily due to the large bar angle, $\alpha \approx 45^\circ$. The axisymmetric oblate bulge model is also only marginally compatible with the observation. The Gaussian ellipsoidal (GE) model clearly best reproduces the observation. It can produce $\tau_{-6} = 6$ if the Galactic bar is very massive ($M = 2.8 \times 10^{10} M_\odot$) and the disk contribution is $\tau_{\text{disk},-6} = 1$. We believe

that the truncated boxy (TB) model is also a viable model. It is therefore desirable to constrain the parameters for this kind of finite truncated bar using the COBE map. From our comparison of the optimal optical depths with the observations, we found the high optical depth already suggests a less than 20° angle between the long axis of the bar and our line of sight to the Galactic centre, and that the axis ratio of the bar is close to the optimal (cf. Fig. 5 and 6).

In our comparison between the prediction and the observation, we have neglected a central nucleus and the dependence of τ on the longitude. The longitude dependence in general reduces the optical depth. But as the mean longitude of the MACHO and OGLE fields are quite small, $l \leq 2.5^\circ$, which corresponds to approximately 375 pc, the reduction is about 20% for the power-law ellipsoidal (PE) model and only about 10% for all the other models. In our Galactic bar models, the density profiles are flat near the Galactic centre, while a nucleus has long been observed in the infrared (Becklin & Neugebauer 1968). But since the MACHO and OGLE fields are all offset by more than 2° from the centre, a nucleus within $2^\circ - 3^\circ$ of the Galactic centre does not affect the microlensing prediction directly except that the nucleus contributes to the dynamical mass within 3 kpc. Including a nucleus would reduce the predicted optical depth outside the nucleus. But we estimate that the mass of the nucleus inside 2° is only about 5% of the total bar mass, much smaller than the uncertainty in the bar and disk mass. So the nucleus can be neglected for predicting optical depth at any field a few degrees ($\gtrsim 3^\circ$) away from the Galactic centre.

In this study, we have used the MACHO and OGLE samples (Alcock et al. 1995b; Udalski et al. 1994). The number of analysed events (50) is still very limited, therefore the errorbars of the inferred optical depths are still quite large. The subsample of (13) clump giant events that we used has even larger errorbars. In addition, some of the long events in the MACHO sample are not well understood and these contribute about 1/3 of the optical depth (Han & Gould 1996). Therefore the current limits on the optical depth have to be interpreted with some caution. Fortunately, the number of events detected toward the Galactic bulge is increasing rapidly with time. In two years, the number of (analysed) microlensing events is likely to increase by four-fold. It will then become feasible to analyse the whole microlensing map of a large fraction of the bulge. If on the order of one hundred events are obtained at two or three low extinction fields close to the minor axis, e.g., the Sgr I field ($1.4^\circ, -2.6^\circ$) and Baade window ($1^\circ, -3.9^\circ$), then we can measure the gradient for the optical depth, which we can use to distinguish bar models with different minor axis profile and boxyness

(cf. Fig. 3). If the optical depth remains high, then tighter limits on the bar parameters can be derived (cf. Figs. 5 and 6). By combining the microlensing map with the event duration distributions, it seems possible to disentangle the relative contributions of the disk and the bar. Furthermore, a comprehensive study combining the information in the gas, stellar kinematics, COBE map and microlensing surveys should provide precise values on all the bar parameters. We conclude that microlensing has become a promising and unique tool in probing the Galactic structures.

This project is partly supported by the ‘‘Sonderforschungsbereich 375-95 f ur Astro-Teilchenphysik’’ der Deutschen Forschungsgemeinschaft. We thank Peter Schneider for comments on the paper.

APPENDIX A: MORE DETAILS OF THE ANALYTICAL MODELS

In this appendix, we give more technical details for the general family discussed in §2.3.

For the density profile described by eqs. (15) and (16), one can show that the central density is given by

$$\rho_0 = \frac{M}{x_0 y_0 z_0} \frac{1}{J(n)K(k)\xi_3(\beta, n)}, \quad (\text{A1})$$

where

$$\xi_3(\beta, n) = \begin{cases} \frac{|\beta - 3|^{\frac{3}{n}}}{n} B\left(\frac{3}{n}, \frac{|\beta| - 3}{n}\right) & \text{if } \beta > 3, \\ \frac{|\beta - 3|^{\frac{3}{n}}}{n} B\left(\frac{3}{n}, \frac{|\beta|}{n} + 1\right) & \text{if } \beta \leq 0, \end{cases} \quad (\text{A2})$$

$$K(k) = \frac{4}{k} B\left(\frac{1}{k}, \frac{1}{k}\right) \approx \frac{8k^2}{k^2 + 1}, \quad (\text{A3})$$

$$J(n) = \frac{2}{n} B\left(\frac{1}{n}, \frac{2}{n}\right) \approx \frac{3n^2}{n^2 + 2}, \quad (\text{A4})$$

where B is the complete Beta-function, and two approximations are given for $K(k)$ and $J(n)$ that are accurate within 3% for $k > 1$ and $n > 1$.

The optical depth at any minor axis field depends on z as follows:

$$\frac{\langle \tau(0, z) \rangle}{\langle \tau(0, 0) \rangle} = \frac{\tau(0, 0, z)}{\tau(0, 0, 0)} = \left[\frac{\rho(0, 0, z)}{\rho(0, 0, 0)} \right]^{1 - \frac{2}{\beta}} = \left[1 + \frac{1}{\beta - 3} \left(\frac{z}{z_0} \right)^n \right]^{-\frac{\beta - 2}{n}}. \quad (\text{A5})$$

The optical depth toward the centre $\langle \tau(0, 0) \rangle$ and the optical depth for a source at the centre $\tau(0, 0, 0)$ are given by

$$\langle \tau(0, 0) \rangle = \tau(0, 0, 0) \xi_1(\beta, n) = \left(\frac{4\pi G}{c^2} \frac{M}{z_0} \right) \xi_0(\beta, n) H\left(k, \frac{y_0}{x_0}, \alpha\right), \quad (\text{A6})$$

where the quantities ξ_0, ξ_1, H are dimensionless functions of the bar angle, shape and radial profile. They are defined as

$$\xi_1(\beta, n) = \frac{\int_{-\infty}^{+\infty} d\lambda f(\lambda) \int_0^{+\infty} d\lambda_1 f(|\lambda - \lambda_1|) \lambda_1}{\int_{-\infty}^{+\infty} d\lambda f(\lambda) \times \int_0^{+\infty} d\lambda_1 f(\lambda_1) \lambda_1}. \quad (\text{A7})$$

$$\begin{aligned} \frac{\xi_0(\beta, n)}{\xi_1(\beta, n)} &= \frac{n}{2|\beta - 3|^{\frac{1}{n}} B(\frac{1}{n}, \frac{|\beta|-3}{n})}, \text{ if } \beta > 3, \\ &= \frac{n}{2|\beta - 3|^{\frac{1}{n}} B(\frac{1}{n}, \frac{|\beta|+2}{n} + 1)}, \text{ if } \beta \leq 0 \\ &\rightarrow \frac{n^{1-1/n}}{2\Gamma(1/n)}, \text{ if } \beta \rightarrow \pm\infty. \end{aligned} \quad (\text{A8})$$

$$H(k, \frac{y_0}{x_0}, \alpha) = \frac{2^{1-\frac{2}{k}}}{K(k)} \left[\frac{1}{\sin 2\alpha} \left(\frac{u^{\frac{k}{2}} + u^{-\frac{k}{2}}}{2} \right)^{-2/k} \right], \quad u \equiv \frac{y_0/x_0}{\tan \alpha}, \quad (\text{A9})$$

where $f(\lambda)$ is defined in eq. (16), and the dependence on the bar angle and axis ratio has been collected in $H(k, y_0/x_0, \alpha)$. For most interesting combinations of β and n , $\xi_1 = (1 \pm 0.1)\sqrt{2}$, and can be approximated within 5% by

$$\xi_1(\beta, n) \approx \frac{4}{3} + \frac{1}{6n} \left(\frac{\beta}{\beta - 3} \right)^{\frac{1}{2}}. \quad (\text{A10})$$

ξ_0 also varies less than 30% from the value for a Gaussian ellipsoidal bar ($\xi_0 = \pi^{-1/2}$) and can be approximated within 15% by

$$\xi_0(\beta, n) \approx \frac{2}{3} \left(1 - \frac{\ln n}{2n} \right) + \frac{1}{12} \left(\frac{\beta}{\beta - 3} \right)^{\frac{1}{2}} \left(1 - \frac{5 \ln n}{n} \right). \quad (\text{A11})$$

The Gaussian ellipsoidal model studied in §2.2 is a special case with $(\beta, n, k) = (\infty, 2, 2)$. For this case, $\xi_1 \rightarrow \sqrt{2}$, $\xi_0 = \pi^{-1/2}$. Another special case is $(\beta, n, k) = (0, \infty, \infty)$, which describes a rectangular homogeneous bar. The result for this model is given in Appendix B.

APPENDIX B: RESULT FOR A HOMOGENEOUS RECTANGULAR BAR

For a homogeneous rectangular bar, $(\beta, n, k) = (0, \infty, \infty)$,

$$\xi_1(\beta, n) = \frac{4}{3}, \quad \xi_0(\beta, n) = \frac{2}{3}, \quad H(k, \frac{y_0}{x_0}, \alpha) = \frac{\min(u, u^{-1})}{4 \sin 2\alpha}, \quad (\text{B1})$$

where u is defined in eq. (A9). Towards the centre,

$$\langle \tau(0, 0) \rangle = \frac{4\pi G}{c^2} \left(\frac{M}{z_0} \right) \frac{1}{6 \sin 2\alpha} \min(u, u^{-1}) \quad (\text{B2})$$

$$= 4 \times 10^{-6} \left(\frac{M}{2 \times 10^{10} M_{\odot}} \frac{0.5 \text{kpc}}{z_0} \right) \min(u, u^{-1}) \frac{1}{\sin 2\alpha} \quad (\text{B3})$$

The optical depth at any field in the $y - z$ plane

$$\begin{aligned} \langle \tau(y, z) \rangle &= \langle \tau(0, 0) \rangle, & \text{if } |y| \leq y_{ic} \text{ and } |z| \leq z_0 \\ &= \langle \tau(0, 0) \rangle \left(\frac{1 - |y|/y_{oc}}{1 - y_{ic}/y_{oc}} \right)^2, & \text{if } y_{ic} < |y| \leq y_{oc} \text{ and } |z| \leq z_0 \\ &= 0, & \text{otherwise,} \end{aligned} \quad (\text{B4})$$

where

$$y_{ic} = |x_0 \sin \alpha - y_0 \cos \alpha|, \quad y_{oc} = x_0 \sin \alpha + y_0 \cos \alpha, \quad (\text{B5})$$

are the y coordinates of two of the four corners of the rectangular bar in the positive y side. Note $\langle \tau(y, z) \rangle$ is independent of y and z in a region near the centre.

APPENDIX C: FIRST ORDER CORRECTION TO THE ANALYTICAL RESULTS

Here we derive a first order correction of our analytical formula for the optical depth, taking into account of the finite distance to the bulge, and the source luminosity function. We show that the first-order correction is zero for the clump giants.

The rigorous expression for the optical depth, as given by eqs. (1) and (2), can be rewritten as:

$$\langle \tau \rangle = \frac{4\pi G}{c^2} \frac{\int_0^{s_{max}} n(D_s) dD_s \int_0^{D_s} dD_d \rho(D_d) D}{\int_0^{s_{max}} n(D_s) dD_s}, \quad n(D_s) dD_s \propto \rho(D_s) \left(\frac{D_s}{R_0} \right)^{2-2\beta_s} dD_s, \quad (\text{C1})$$

where the symbols are the same as in eqs. (1) and (2), and R_0 is the distance to the Galactic centre.

To the first order of $\left(\frac{a}{R_0} \right)$, where a is a characteristic length scale of the bar,

$$D \approx (x_s - x_l) \frac{R_0 + x_l}{R_0 + x_s} \approx (x_s - x_l) - \frac{(x_s - x_l)^2}{R_0}, \quad (\text{C2})$$

and

$$n(D_s) dD_s \propto \rho(D_s) dD_s \left(1 + \frac{x_s}{R_0} \right)^{2-2\beta_s} \propto \rho(D_s) dD_s \left[1 + (2 - 2\beta_s) \frac{x_s}{R_0} \right]. \quad (\text{C3})$$

Changing the lens and source coordinates to the (x, y, z) frame, and assuming the density of source or lens is zero at the large radius, we have

$$\langle \tau \rangle \approx \langle \tau_1(y, z) \rangle = \frac{4\pi G}{c^2} \frac{I_2 + I_3}{I_0 + I_1}, \quad (\text{C4})$$

where

$$I_0 = \int_{-\infty}^{+\infty} dx_s \rho(x_s, y, z), \quad (\text{C5})$$

$$I_2 = \int_{-\infty}^{+\infty} dx_s \rho(x_s, y, z) \int_{-\infty}^{x_s} \rho(x_l, y, z) (x_s - x_l) dx_l, \quad (\text{C6})$$

and

$$I_1 = 2(1 - \beta_s) \int_{-\infty}^{+\infty} dx_s \frac{x_s}{R_0} \rho(x_s, y, z), \quad (\text{C7})$$

$$= -2(1 - \beta_s) \int_{-\infty}^{+\infty} dx_s \frac{x_s}{R_0} \rho(x_s, -y, z), \quad (\text{C8})$$

$$= (1 - \beta_s) \int_{-\infty}^{+\infty} dx_s \frac{x_s}{R_0} [\rho(x_s, y, z) - \rho(x_s, -y, z)], \quad (\text{C9})$$

$$= 0, \quad \text{if } y = 0 \text{ or } \beta_s = 1, \quad (\text{C10})$$

$$I_3 = \int_{-\infty}^{\infty} dx_s \int_{-\infty}^{x_s} dx_l \rho_{+,+y} \left[-\frac{(x_s - x_l)^2}{R_0} + 2(1 - \beta_s) \frac{x_s(x_s - x_l)}{R_0} \right] \quad (\text{C11})$$

$$= \int_{-\infty}^{\infty} dx_s \int_{-\infty}^{x_s} dx_l \rho_{-, -y} \left[-\frac{(x_s - x_l)^2}{R_0} + 2(1 - \beta_s) \frac{x_l(x_l - x_s)}{R_0} \right] \quad (\text{C12})$$

$$= (1 - \beta_s) \int_{-\infty}^{\infty} dx_s \int_{-\infty}^{x_s} dx_l \rho_{\text{odd}} \left[\frac{x_s^2 - x_l^2}{2R_0} \right] \quad (\text{C13})$$

$$- \beta_s \int_{-\infty}^{\infty} dx_s \int_{-\infty}^{x_s} dx_l \rho_{\text{even}} \left[\frac{(x_s - x_l)^2}{2R_0} \right]$$

$$= -\beta_s \int_{-\infty}^{\infty} dx_s \int_{-\infty}^{x_s} dx_l \rho(x_s, 0, z) \rho(x_l, 0, z) \left[\frac{(x_s - x_l)^2}{R_0} \right], \quad \text{if } y = 0, \quad (\text{C14})$$

where

$$\rho_{+,+y} = \rho(x_s, y, z) \rho(x_l, y, z), \quad \rho_{-, -y} = \rho(x_s, -y, z) \rho(x_l, -y, z), \quad (\text{C15})$$

$$\rho_{\text{even}} = \rho_{+,+y} + \rho_{-, -y}, \quad \rho_{\text{odd}} = \rho_{+,+y} - \rho_{-, -y}. \quad (\text{C16})$$

In the above we have used $\langle \tau_1(y, z) \rangle$ to denote the first order corrected optical depth. If we use $\langle \tau_0(y, z) \rangle$ to denote the optical depth given by eq. (4) in the main text, then $\langle \tau_1(y, z) \rangle$ reduces to $\langle \tau_0(y, z) \rangle$ if the first order correction terms I_1 and I_3 are set to zero.

Eqs. (C8) and (C12) are derived by applying a change of the dummy variables

$$x_s \rightarrow -x_l, \quad x_l \rightarrow -x_s, \quad (\text{C17})$$

and the central symmetry of bars

$$\rho(-x, y, z) = \rho(x, -y, z), \quad (\text{C18})$$

to eqs. (C7) and (C11). We then obtain eqs. (C9) and (C13) after adding eqs. (C7) and (C8), and eqs. (C11) and (C12), and then dividing both sides by two. Eq. (C14) is because $\rho_{\text{odd}} = 0$ on the minor axis.

A nice result from this is that for red clump stars with presumably $\beta_s = 0$, $I_1 = I_3 = 0$ for any line-of-sight along the minor axis $y = 0$. Hence $\langle \tau_1(0, z) \rangle = \langle \tau_0(0, z) \rangle$, namely, the

optical depth given in the main text is correct to the first order. This conclusion is true for any bar density profile, shape and orientation.

For main sequence sources with $\beta_s > 0$, our formula over-estimates the optical depth and has to be corrected down. For the density profiles described by eqs. (15) and (16), after some tedious algebra, the optical depth, corrected to first order, is given by

$$\langle \tau_1(0, z) \rangle = \langle \tau_0(0, z) \rangle \left(1 + \frac{I_3}{I_2} \right) = \langle \tau_0(0, z) \rangle \left[1 - \xi_4 \beta_s \frac{a}{R_0} \left(\frac{\rho(0, 0, z)}{\rho(0, 0, 0)} \right)^{-\frac{1}{\beta}} \right] \quad (\text{C19})$$

$$= \langle \tau_0(0, z) \rangle \left(1 - \xi_4 \beta_s \frac{a}{R_0} \left[1 + \frac{1}{\beta - 3} \left(\frac{z}{z_0} \right)^n \right]^{\frac{1}{n}} \right), \quad (\text{C20})$$

where

$$\frac{1}{a^k} = \frac{\cos^k \alpha}{x_0^k} + \frac{\sin^k \alpha}{y_0^k}, \quad \xi_4(\beta, n) \approx 3^{\frac{1}{n}}. \quad (\text{C21})$$

The expression for $\xi_4(\beta, n) \approx 3^{\frac{1}{n}}$ is accurate within 15% for most bar models, and is exact for homogeneous ($\beta = 0$) bar. For Gaussian ellipsoidal bars, $\xi_4 = \sqrt{\pi}$. Other exact values for ξ_4 for a few models are given in Table 1. From eq. (C20), the first-order correction is bigger away from the plane for power-law models ($\beta > 3$), smaller for truncated bars ($\beta \leq 0$) and independent of z for $\beta \rightarrow \infty$ (e.g., the Gaussian and exponential models).

We have also checked these formulae with fully numerical calculations. We find that the above first order corrected results hold within 5%-15% for the full range of models discussed in the main text, which have $a/R_0 \leq \frac{1}{4}$.

For readers' convenience, we summarize in the following how to use our analytical formulae:

(i) Find the value of $\xi_0(\beta, n)$. ξ_0 for six combinations of (β, n) are tabulated in Table 1. For combinations not found in the table, the approximation given by eq. (A11) should be sufficient for most cases. When more accuracy is desired, use eqs. (A7) and (A8).

(ii) Use eq. (A9) to calculate the function $H(k, y_0/x_0, \alpha)$.

(iii) Now use eq. (27) to calculate the zeroth-order optical depth.

(iv) The first order corrected optical depth can be obtained using eqs. (C21) and (C20).

REFERENCES

- Alard, C. et al. 1995, *The Messenger*, 80, 31
 Alcock, C. et al. 1993, *Nature*, 365, 621
 Alcock, C. et al. 1995a, preprint (astro-ph/9506113)
 Alcock, C. et al. 1995b, preprint (astro-ph/9512146)

- Aubourg, E., et al. 1995, *Nature*, 365, 623
- Becklin, E. E. & Neugebauer, G., 1968, *ApJ*, 151, 145.
- Binney, J. et al. 1991, *MNRAS*, 252, 210
- Blitz, L., & Spergel, D. N. 1991, *ApJ*, 379, 631
- Blum, 1995, *ApJ*, 444, L89
- Dwek, E. et al. 1995, *ApJ*, 445, 716
- Gerhard, O. E. & Vietri, M. 1986, *MNRAS*, 223, 277
- Gould, A., Bahcall, J.N., & Flynn, C. 1996, *ApJ*, 465
- Han, C. & Gould, A. 1996, *ApJ*, submitted (= astro-ph/9504078)
- Han, C. & Gould, A. 1995, *ApJ*, 449, 521
- Holtzman, J.A. et al. 1993, *AJ*, 106, 1826
- Kent, S. M., 1992 *ApJ*, 387, 181
- Kiraga, M. & Paczyński, B. 1994, *ApJ*, 430, 101
- Paczynski, B. et al. 1994a, *ApJ*, 435, L113
- Paczynski, B. et al. 1994b, *AJ*, 107, 2060
- Paczynski, B. 1996, *ARAA*, 34, in press
- Sellwood, J. & Wilkinson, A., 1993, *Rep. Prog. Phys.*, 56, 173.
- Stanek, K. Z. et al. 1994, *ApJ*, 429, L73
- Udalski, A. et al. 1993, *AcA*, 43, 289
- Udalski, A. et al. 1994, *AcA*, 44, 165
- Weiland, J. et al. 1994, *ApJ*, 425, L81
- Zhao, H. S. 1996, *MNRAS*, submitted
- Zhao, H. S., Rich, R. M. & Spergel, D. N. 1996, *MNRAS*, in press (ZRS96)
- Zhao, H. S., Spergel, D. N., & Rich, R. M. 1995 *ApJ*, 440, L13 (ZSR95)

This paper has been produced using the Royal Astronomical Society/Blackwell Science L^AT_EX style file.